# Journal Pre-proof

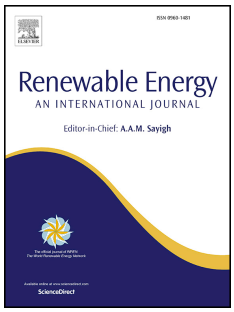


Estimating annual energy production from short tidal current records

Tongtong Xu, Kevin A. Haas, Budi Gunawan

PII: S0960-1481(23)00258-6

DOI: https://doi.org/10.1016/j.renene.2023.02.107

Reference: RENE 18427

To appear in: *Renewable Energy*

Received Date: 4 March 2022

Revised Date: 9 February 2023

Accepted Date: 21 February 2023

Please cite this article as: Xu T, Haas KA, Gunawan B, Estimating annual energy production from short tidal current records, *Renewable Energy* (2023), doi: https://doi.org/10.1016/j.renene.2023.02.107.

**Tongtong Xu:** Methodology, Formal Analysis, Writing- Original draft preparation. **Kevin Haas**: Conceptualization, Supervision, Writing- Reviewing and Editing. **Budi Gunawan**: Project Administration, Funding Acquisition, Writing- Reviewing and Editing,

# Estimating annual energy production from short tidal current records

**Tongtong Xu[a,b], Kevin A. Haas[c], Budi Gunawan[d]**

*[a]NOAA Physical Sciences Laboratory, Boulder, CO.*

*[b]CIRES, University of Colorado, Boulder, CO.*

*[c]School of Civil and Environmental Engineering, Georgia Institute of Technology, Atlanta, US.*

*[d]Water Power Technologies, Sandia National Laboratories, Albuquerque, US.*

[*]Corresponding Author

Kevin A. Haas

Email: kevin.haas@ce.gatech.edu

Address: 790 Atlantic Dr NW, Atlanta, GA 30332

**Highlights:**

1. The accuracy of annual energy production (AEP) estimation does not necessarily improve with the use of a longer tidal current record for its calculation
2. Computed AEP uncertainties are in resonance with relevant astronomical influences
3. AEP assessment is improved by following optimal strategies for short record measurements

Submitted to Renewable Energy

February, 2023

**Abstract:**

Deploying Tidal Energy Converters for electricity generation requires prior-knowledge of the potential Annual Energy Production (AEP) at the site. Ideally, using a year-long tidal current record at the proposed site to minimize uncertainty. However, such records are often unavailable. Fortunately, using the periodic nature of tidal variability, the International Electrotechnical Commission Technical Specification for tidal energy resource assessment requires AEP calculation using at least 90 days of tidal current records at each turbine location. The sensitivity of AEP to different record durations has not been fully assessed. This is the goal of our study. The study utilized the U.S. tidal energy geodatabase to simulate tidal currents with various lengths, during 100 years of the 21$^{st}$ century. We then consider two frameworks for evaluating AEP: (a) The long-term (months) fixed instrument (FI) measurement at each proposed tidal turbine location, and (b) one FI measurement and short-term (hours) boat-based moving vessel measurements. Under the two scenarios, we examine the AEP assessed from short tidal current records, including how the AEP uncertainties vary spatially and temporally, and how they are associated with various astronomical factors. This helps provide guidance on choosing the appropriate assessment methodologies to reduce the AEP uncertainties and project cost.

**Keywords:**

Tidal energy converters; synthetic tidal currents; annual energy production; statistical uncertainty; least square regression; astronomical influence

## 1. Introduction

The continuously growing global energy demand has been mainly met by fossil fuel combustion, leading to expansion of carbon emission and exacerbation of global warming [1].

To constrain the global warming to 1.5°C above pre-industrial level, the renewable share in electricity generation is required to reach 50% by 2030 and 70% by 2050 [2]. In 2020, 29% of electricity generation is supplied by renewables [1] (26% in 2018 [3]), among which solar and wind energy are the major contributors and projected to continuously expand in the near future [4]. Tidal energy has the potential for becoming a contributor to the renewable energy portfolio due to its predictability and the constantly improving technology for extraction, making it a potentially reliable and dependable energy source.

Tides are the regular rise and fall of the ocean surface and the induced currents, derived from the gravitational and centrifugal force balance between the earth, moon, and sun [5]. A lunar day (24 hours and 50 minutes) is the time it takes for a fixed point on earth to complete a rotation under the same point on the moon. Correspondingly, the forces on that point changes from the strongest gravitational pull of the moon to the strongest centrifugal force, generating two high tides per day [6]. The existence of continents greatly interferes with the surging process, resulting in distinct tidal characteristics, including (a) semidiurnal tides, featured by two high tides and two low tides per day, (b) diurnal tides, i.e., daily occurrence of one high tide and one low tide, and (c) mixed tides, having signatures in between [7]. Twice per month during a lunar month (29.53 days), the moon orbits around the earth to a position that the moon, sun and earth are nearly in alignment, where the gravitational forces of the moon and the sun are superimposed, leading to higher-than-average tidal ranges, denoted as spring tides [8]. Neap tides, referring to lower tidal ranges, also occur twice a month when the sun and moon are aligned at a right angle from the earth. The long-term tidal variation is modulated by the 18.61-year lunar nodal cycle. The orbit of the moon is inclined at a constant 5° 9’ to the ecliptic, the plane in which the earth orbits the sun, whereas the earth’s equatorial plane is inclined at a

constant $23^{o}\,27'$ to the ecliptic. The resulting lunar declination, the angle of the lunar orbit to the equator, is dynamically changing, reaching to a maximum ($23^{o}\,27'+5^{o}\,9'$) and a minimum ($23^{o}\,27'-5^{o}\,9'$) once every 18.61 years, which leads to the largest nodal modulation of diurnal tides and semidiurnal tides, respectively [9-11]. Due to these astronomical formations, tides are inherently periodic and predictable, making tidal energy available on a consistent basis, which is a desired feature for reliable energy generation.

Tidal energy includes both tidal range and tidal stream energy, extracted from the regular rise and fall of the ocean surface and the induced current, respectively. Presently, tidal range energy has been harnessed on a commercial scale using tidal barrages, designed to create an artificial phase difference by impounding water and subsequently allowing it to flow through turbines [12]. However, due to the high cost of constructing a dam and potentially significant environmental impacts from damming, only several commercial tidal barrages are currently present, in France [13], Russia [6], Canada [14], China [15], and Korea [16]. In contrast, extracting tidal stream energy directly from the moving water with Tidal Energy Converters (TECs) requires less infrastructure and allows more flexible site selections. As such, much of the ongoing development has been devoted to tidal stream technology. Prototype and pioneering devices have been tested in several demonstration sites, including: the US Federal Energy Regulatory Commission Pilot Project-licensed Roosevelt Island Tidal Energy project at New York City's East River [17, 18]; the Zhoushan experiment in China [19]; the MeyGen project in Scotland [20]; the Orbital Marine Power's floating tidal energy commercialization project, Scotland, that supports the electricity needs of approximately 830 UK homes in 2020 [20]. Their upgraded in-operation O2 turbine since summer 2021 aims to provide annual electricity to 2000 UK homes [21, 22].

When determining the suitability of tidal stream sites, comprehensive regional resource assessments should be performed to evaluate the Annual Energy Production (AEP). The European Marine Energy Centre in 2009 [23] and the International Electrotechnical Commission in 2015 (hereinafter referred to as IEC-62600-201) [24] have outlined a unified technical specification, regarding modeling, measurement, and analysis of the AEP based on tidal current records. For the purpose of computing the AEP, the technical specification recommends a minimum in-situ measurement of 90 days whereas the minimum hydrodynamic simulation needs to be one year. In addition, the tidal current variation of the measured or simulated time period should be comparable to the tidal current variation in a typical year. The term "typical" refers to a period of time with little nodal effect, as opposed to strong nodal modulation, which we will show accounts for ~10 % of the AEP estimation uncertainty. Hence, the technical specification has acknowledged the uncertainties of the AEP estimation from short tidal current records; however, the quantification of these uncertainties has not been completed.

In numerical and observational studies that adopt the guidelines of the technical specification (e.g., [25, 26]), the uncertainties of the AEP estimation are rarely extensively discussed. One exception is the Admiralty Inlet tidal characterization, U.S. [27], which explicitly analyzed how the mean power density estimated from increasingly longer records gradually approaches the actual annual evaluation. Another example is the Alderney Race tidal characterization, France [28], which quantifies the decadal variability of AEP modulated by the lunar nodal cycle. In addition, an assessment of AEP in north-western Europe has documented that the lunar nodal cycle can contribute up to 10% AEP uncertainty [29], consistent with studies focusing on several other regions (see references in [29]). Yet these are site specific regional studies, which may not be sufficient to deliver general conclusions on the AEP uncertainties.

To compensate for the lack of uncertainty analysis in the first edition IEC-62600-201, an IEC Maintenance Team (MT) is working to expand on the unresolved issues. Besides quantifying the AEP uncertainties estimated directly from short tidal current records, an equally relevant topic is to explore indirect AEP computations, referring to (a) projecting a high-resolution long-term tidal current record at one location onto a nearby location with a tidal record of hours, and subsequently (b) assessing the AEP of the nearby location from the inferred long-term tidal record. One example is Ref. [30]. The indirect method, if robust, can be particularly useful and cost effective for assessing the AEP of TEC arrays by greatly reducing the number of required instruments and measurement durations.

Given the aforementioned unresolved issues regarding AEP uncertainties, here our study focuses on conducting comprehensive AEP uncertainty assessment *directly or indirectly* derived from short tidal current records. For tidal data, we utilize the pre-validated U.S. tidal energy geodatabase [31] containing over 3.6 million geographic locations and their harmonic constituents, to generate a large quantity of long-term tidal records. The geodatabase allows us the flexibility to explore many potential options of single TEC and TEC arrays deployment, for which we analyze the uncertainties associated with direct and indirect AEP assessment, respectively. Through this analysis, we aim to (a) quantify the uncertainties of AEP assessment, including their spatial distribution and temporal variation, (b) improve our understanding on how the uncertainties are related to the astronomical sources, and (c) provide statistically robust guidelines on best practices for future measurements and choosing the most appropriate assessment methodologies for computing AEP.

## 2. Data and Methods

### 2.1 Data

We obtained the U.S. tidal energy geodatabase [31] containing 3.6 million geographic locations and their water depths, depth-averaged mean current magnitudes, dominant water level and tidal current constituents, including semidiurnal ($M_2$, $N_2$, $S_2$), diurnal ($K_1$, $O_1$, $Q_1$) constituents and shallow water harmonics ($M_4$ and $M_6$). The geodatabase was built from multiple simulations of the U.S. coastal waters, using the Regional Ocean Modeling System (ROMS) [32], a well-known three-dimensional free-surface terrain-following numerical model. All ROMS subdomains have an average grid spacing of at least 350 m within the inshore regions of interest; only the aforementioned tidal constituents were simulated, although nodal corrections were included in creating the forcing for the model (see [31] for details regarding the geodatabase). Because the present study is focused on the methodologies rather than performing the actual tidal energy resource assessment, the model resolution and number of constituents provide enough detail to evaluate the effectiveness of the methods.

The constituents were processed by T-TIDE [33], a Matlab toolbox of a standard harmonic-based prediction method. These constituents were then used to generate depth-averaged tidal current and water level records of various durations during the 21$^{st}$ century, using the function "t_predic" of the T-TIDE toolbox. The nodal corrections based on the latitude are included by T-TIDE when creating the time series.

### 2.2 Direct AEP assessment of single TECs

The theoretical output power of a TEC is related to the kinetic energy of the currents [34]. The power per unit area ($W/m^2$), without considering the turbine efficiency and other potential losses in power extraction, is given by,

$$\mathrm{p} = \frac{1}{2}\rho \mathrm{U}^3, \quad (1)$$

where $\rho = 1025\ kg/m^3$ is the density of seawater, and U is the depth-averaged horizontal current velocity. We also do not consider the potential tidal phase differences across the water column, which may cause tidal currents at different water depths reaching peak current magnitudes at a different time. Our results thus represent the depth-averaged and theoretical AEP assessment.

To estimate the AEP of a potential TEC site, a current magnitude time series at the site, $\mathrm{U}(t)$, is processed into velocity bins to compute the discrete probability distribution, denoted as,

$$f_i = \mathrm{P}(\mathrm{U}_{i-1} \le \mathrm{U}(t) < \mathrm{U}_i), \quad (2)$$

where $\mathrm{U}_i$ is the $i$-th bin of $\mathrm{U}(t)$, $f_i$ is the probability of $\mathrm{U}(t)$ between $\mathrm{U}_{i-1}$ and $\mathrm{U}_i$, $i$ ranges from 1 to $N$, and $N$ is the total number of bins. $N = 20$ in this study, and the velocity bins were evenly distributed from 0 to maximum of $\mathrm{U}(t)$. The bin width is $\max\big(\mathrm{U}(t)\big)/20$, in which the maximum is derived directly from the current magnitude time series of the site. $\mathrm{U}(t)$ is obtained through "t_predic" (see section 2.1).

According to IEC-62600-201 [24], the AEP with the unit of $kW \cdot hr$ is determined as the weighted sum of the power produced by each velocity bin, multiplied by the total hours per year ($N_h = 8760$ hours), as followed,

$$\mathrm{AEP} = \frac{N_h}{1000} \cdot \sum_{i=1}^{N} \mathrm{p}_i \cdot f_i, \quad (3)$$

where $\mathrm{p}_i$ is computed from (1) with $\mathrm{U} = \frac{1}{2}(\mathrm{U}_{i-1} + \mathrm{U}_i)$. The 1000 converts W into kW. [Note that the current magnitude time series is denoted as $\mathrm{U}(t)$=$\sqrt{u(t)^2 + v(t)^2}$, whereas $\vec{\mathrm{U}}(t) =$

154 $u(t) + i \cdot v(t)$ denotes the current time series with real and imaginary parts being zonal and
155 meridional current components, respectively.]

156 To compare the AEP estimated from a short record to that from a full-year record, we adopt
157 the relative AEP error,

$$\mathrm{dAEP} = \frac{\widehat{\mathrm{AEP}} - \mathrm{AEP}}{\mathrm{AEP}} \times 100\%, \quad (4)$$

158 where $\widehat{\mathrm{AEP}}$ is the short-record estimation, and AEP is the reference from a full year. We chose
159 2012 as our reference, considering that 2012 is a year of limited nodal cycle influence where the
160 AEP computed for that year is close to the 18-year average.

161 To robustly assess the uncertainty of AEP induced by short-record tidal currents, we
162 analyzed dAEP for many locations and time periods with various durations. Specifically, from
163 the tidal database [31], we extracted 5338 moderate energy locations with mean current
164 magnitude $\geq 0.5$ m/s. We also identified 395 high energy locations with mean current magnitude
165 $\geq 1$ m/s. In addition, all moderate energy and high energy locations have water depths $\geq 5$ m,
166 and a minimum distance between any two locations $\geq 2$ km. The spatial distribution of these
167 locations is shown in Figure 1. For each selected location, we generated the full-year-long 2012
168 tidal current record with a temporal resolution of 30 mins; this is used to derive the reference
169 AEP in (4). We then randomly generated 500 timestamps between the year 2000 and the year
170 2100, following the uniform distribution (i.e., equal probability of sampling any timestamp). We
171 then generated a tidal current record that starts from each of those timestamps and ends after $d$
172 days; $d$ thus represents the duration of the sampled record. This results in 500 short records of $d$-
173 day tidal currents, upon which we evaluate $\widehat{\mathrm{AEP}}$ used in (4) and derive dAEP. The above process
174 is carried out for each location of interests, leading to a dAEP matrix of size $5338 \times 500$ for
175 moderate energy locations (size $395 \times 500$ for high energy locations). We find that, in our

176 synthetic record analysis, sampling 500 tidal records sufficiently captures the tidal variability
177 during the 21st century.
178

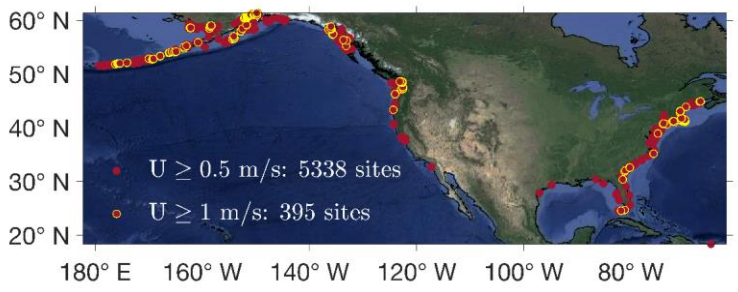


179
180 Figure 1. Spatial distribution of moderate energy sites (red circles) and high energy sites (red
181 circles with yellow edge) of interest.
182

183 Furthermore, we examined multiple options of short durations, to comprehensively evaluate
184 the AEP uncertainties and to search for the optimal choices of durations that lead to more
185 accurate AEP assessment. Durations of short records that we examined range from 14 to 196
186 days, which covers much shorter to much longer than the 90-day requirement specified by the
187 IEC-62600-201. Incorporating the durations, the dAEP matrix can be generally represented as
188 dAEP$(s, \tau, d)$, where $s$ represents a location, $\tau$ represents center of the time period being
189 examined, and $d$ is the duration of that time period.
190 We then analyzed the spatial and temporal variation of the AEP assessment uncertainty,
191 primarily based on this dAEP$(s, \tau, d)$ matrix. For example for $d = 90$ days, we computed the
192 95% confidence interval of the dAEP$(s, \tau, d = 90$ days$)$ matrix along the $\tau$ dimension, while
193 fixing the location $(s)$. Repeating this computation for every location thus gives us the AEP
194 uncertainty at every location of interest. We also derived the 95% confidence interval of the

dAEP$(s, \tau, d = 90 \text{ days})$ matrix along the $s$ dimension, while fixing the time period ($\tau$) being examined. Repeating this computation for every sampled time period provides us the AEP uncertainty as a function of time.

### 2.3 Regression-based AEP assessment of TEC arrays

Utility-scale tidal energy plants often need to contain an array of turbines. To be able to assess the AEP of the array, a sufficiently long tidal current record at each TEC location is required. Conducting long-term direct measurements at each individual TEC location using current profilers can be cost prohibitive, especially if a large number of TECs is proposed for the site. As a means to reduce measurement cost, we propose conducting indirect measurements using only two current profilers for assessing the AEP of an array. The two current profilers consist of a bottom-mounted one deployed for a sufficiently long period of time at one proposed TEC location, and a surface vessel mounted one that periodically measures the current at the other proposed TEC locations within the array for a very short period of time. From this point forward, the bottom mounted current profiler is termed as fixed instrument (FI) and the vessel mounted one is termed as moving vessel (MV) measurement (an example shown in Figure 2a).

211

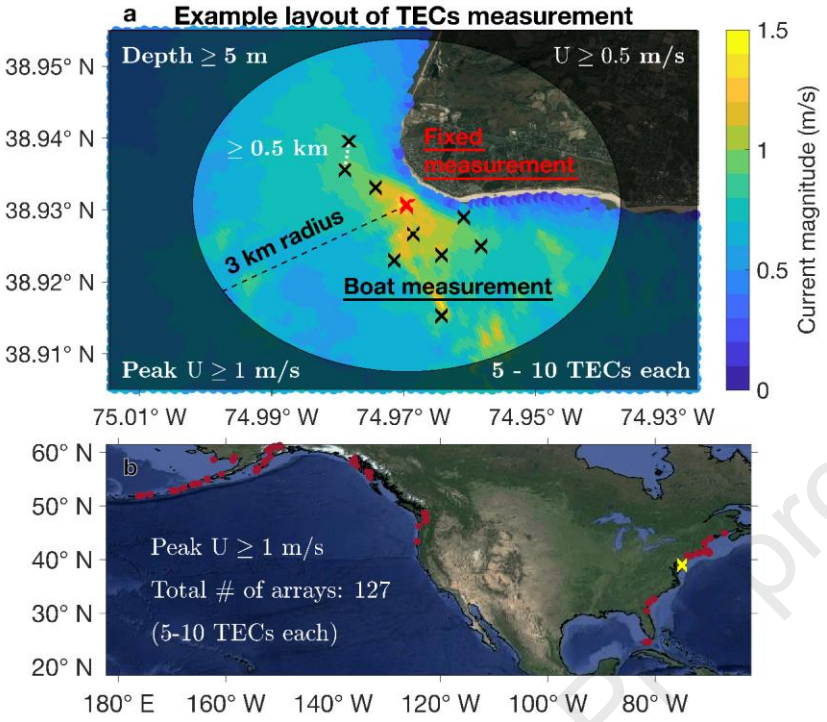


212

213 Figure 2. Example layout of defining the array of potential Tidal Energy Convertors (TECs) and
214 the spatial distribution of all arrays analyzed. (a) At a pre-defined site (a highlighted circle of a 3
215 km radius) containing at least one location of mean current magnitude ≥ 1 m/s, the highest
216 velocity location is selected for FI measurement (red cross); the nearby high velocity locations
217 are set for MV measurements (black cross). Color contours are the mean current magnitude. The
218 array of TECs consists of the FI measurement and the MV measurement locations. All TECs
219 have the mean current magnitude ≥ 0.5 m/s, the water depth ≥ 5 m, and a minimum distance
220 between any pair of locations ≥ 0.5 km. (b) Spatial distribution of 127 arrays of TECs (red dots)
221 defined from the tidal database, with each array containing 5-10 TECs. Yellow cross marks the
222 geographic location of the example in (a).

223

The suitability of using the proposed indirect method is analyzed herein using the synthetic data from the U.S. tidal energy geodatabase [31]. The FI measurement is represented using a full-year-long tidal time series with high temporal resolution ($\Delta t = 6$ min) at a location. The MV measurements are represented using short time records, with durations spanning a total length of hours at each of the TEC locations ($\Delta t = 1$ hour). A full-year-long tidal current record at each MV measurement location is then inferred from the FI measurement, through a least-square regression method.

Recall that the IEC-62600-201 [24] standard requires only a 90-day measurement record. In this study testing the regression-based indirect measurement method, we assume a year-long tidal time series in a year of limited nodal cycle influence at the FI measurement location (i.e., minimizing the uncertainty linked to the FI measurement). This allows us to isolate the AEP uncertainty associated with the indirect method, from the uncertainty associated with the direct (FI) measurement. By separately assessing the AEP uncertainty in both methods, we then make recommendations on the optimal durations of FI measurement and MV measurement (see Discussion and Conclusion).

Also, tidal current records, whether they represent the FI or the MV measurement, are all obtained by processing the tidal constituents of the geodatabase through "t_predic". Note that "t_predic" allows generation of tidal records with any specified temporal resolution. To make these records more realistically represent the measurement obtained from the field, the temporal resolution of the FI measurement is set at $\Delta t = 6$ min, to resemble the sampling frequency of the FI current profilers repeatedly measuring a fixed water column. It is important to note that the FI temporal resolution needs to have a $\Delta t$ less than or equal to the MV temporal resolution. For this case, the temporal resolution of the MV measurement is set at $\Delta t = 1$ hour. Realistically for a

properly assigned TEC array, a moving vessel can circulate around all TEC locations in an hour, during which each TEC location is measured for several minutes and an average current speed is computed, hence the approximately 1-hour resolution at each TEC.

With the synthetic FI and MV records, we build the least-square regression modelling framework as follows,

$$\begin{bmatrix} \mathbf{y}_1(t) \\ \mathbf{y}_2(t) \\ \vdots \\ \mathbf{y}_M(t) \end{bmatrix} = \mathbf{L}\mathbf{x}_0(t), \tag{5}$$

where $\mathbf{L}$ is the linear operator to be solved, $\mathbf{x}_0(t)$ denotes the FI record at location 0, $\mathbf{y}_j(t)$ is the MV record at $j$-th TEC location of the array, $j$ ranges from 1 to $M$, where $M$ is the total number of TEC locations surveyed using MV measurements. The total number of TEC locations at a given site is equal to $M + 1$, including MV and FI measurements.

The solution of $\mathbf{L}$ relies on having identical timestamps for the MV and FI records, which is achieved by interpolating the FI record onto the same timestamps of the MV measurements. More realistically, as the vessel carrying the current profiler revisits the MV locations periodically, the MV measurement timestamps differ between TEC locations. Thus, the FI record is individually interpolated onto timestamps of each MV measurement location. Then we solve $\mathbf{L}$ as,

$$\mathbf{L} = \begin{bmatrix} \mathbf{y}_1(t_{b_1})\mathbf{x}_0(t_{b_1})^{\mathrm{H}} / \left(\mathbf{x}_0(t_{b_1})\mathbf{x}_0(t_{b_1})^{\mathrm{H}}\right) \\ \mathbf{y}_2(t_{b_2})\mathbf{x}_0(t_{b_2})^{\mathrm{H}} / \left(\mathbf{x}_0(t_{b_2})\mathbf{x}_0(t_{b_2})^{\mathrm{H}}\right) \\ \vdots \\ \mathbf{y}_M(t_{b_M})\mathbf{x}_0(t_{b_M})^{\mathrm{H}} / \left(\mathbf{x}_0(t_{b_M})\mathbf{x}_0(t_{b_M})^{\mathrm{H}}\right) \end{bmatrix}, \tag{6}$$

where $t_{b_j}$ is the timestamps at $j$-th MV measurement location, and $^{\mathrm{H}}$ is the conjugate transpose. Note that if the time series is real, $^{\mathrm{H}}$ is equivalent to $^{\mathrm{T}}$, the transpose. In this synthetic study, we

generate MV measurement time series such that $t_{b_1} = t_{b_2} = \cdots = t_{b_M}$, and each timestamp of $t_{b_j}$ has an exact match in $t_f$, the timestamps of the FI record (i.e., no interpolation involved).

The inferred long-term time series at MV measurement locations are obtained by,

$$\begin{bmatrix} \hat{\mathbf{y}}_1(t_f) \\ \hat{\mathbf{y}}_2(t_f) \\ \vdots \\ \hat{\mathbf{y}}_M(t_f) \end{bmatrix} = \mathbf{L}\mathbf{x}_0(t_f), \tag{7}$$

where $\hat{\mathbf{y}}_j(t_f)$ is the inferred tidal record at $j$-th location.

The array AEP is the summation of the individual-location AEP, $\sum_{j=0}^{M} \widehat{\mathrm{AEP}}_j$, estimated from each inferred record and the FI record. This is compared with the reference array AEP, $\sum_{j=0}^{M} \mathrm{AEP}_j$, obtained from the full-year "true" records of the geodatabase. Thus, the relative error of array AEP is defined accordingly as,

$$\mathrm{dAEPs} = \frac{\sum_{j=0}^{M} \widehat{\mathrm{AEP}}_j - \sum_{j=0}^{M} \mathrm{AEP}_j}{\sum_{j=0}^{M} \mathrm{AEP}_j} \times 100\%. \tag{8}$$

For robust assessment of the AEP uncertainty associated with the regression-based method, we defined 127 tidal energy sites (each site consists of an array of TECs, Figure 2b). We selected a TEC array following a similar strategy as for selecting a single TEC (see Section 2.2); that is, for each array, at least one TEC location has a mean current magnitude $\geq 1$ m/s, and all locations have a mean current magnitude $\geq 0.5$ m/s, a water depth $\geq 5$ m, and any pair of TEC locations is separated by a distance of at least 0.5 km and at most 6 km. We generated the full-year-long (2012) tidal current and water level records at each TEC location of each tidal energy site. At each site, one TEC location is selected as the FI location and the sensitivity of the choice of the FI location is explored in this analysis and will be discussed. The rest of the sites are the MV measurement locations, at each of which we randomly generated 500 timestamps from the 2012

records. The tidal current records that start from these sampled timestamps were then extracted with 1-hour sampling rate. Record durations vary from 12 to 240 hours. From these, we computed a $\mathrm{dAEPs}(a,\tau,d)$ matrix of size $127\times 500\times 228$. [$a$ denotes the index of the TEC array.]

For the regression framework, different combinations of input variables that we examined include (a) the velocity magnitude, $\mathbf{x}_0(t)=\mathrm{U}_0(t)$, (b) the velocity magnitude and water level $\eta_0(t)$, i.e., $\mathbf{x}_0(t)=\begin{bmatrix}\mathrm{U}_0(t)\\ \eta_0(t)\end{bmatrix}$, (c) the velocity vector , $\mathbf{x}_0(t)=\vec{\mathrm{U}}_0(t)$, (d) the velocity vector and water level, $\mathbf{x}_0(t)=\begin{bmatrix}\vec{\mathrm{U}}_0(t)\\ \eta_0(t)\end{bmatrix}$, (e) the cubic velocity magnitude, $\mathbf{x}_0(t)=\mathrm{U}_0(t)^3$, and (f) the cubic velocity magnitude and water level, $x_0(t)=\begin{bmatrix}\mathrm{U}_0(t)^3\\ \eta_0(t)\end{bmatrix}$. Correspondingly, the output variables vary: (a-b) $\mathbf{y}_j(t)=\mathrm{U}_j(t)$, (c-d) $\mathbf{y}_j(t)=\vec{\mathrm{U}}_j(t)$, (e-f) $\mathbf{y}_j(t)=\mathrm{U}_j(t)^3$, i.e., in the same format as the velocity component of the inputs. Thus, the AEP error matrix is expanded to $\mathrm{dAEPs}(a,\tau,d,q)$. [$q$ denotes the option of regression framework.] These options allow us to examine the optimal combination of variables, which helps us evaluate the robustness of the regression-based array AEP assessment. Because the regression is applied at each TEC location, this will account for the spatial variability of the velocity and water level. Note that for all of these options, we examine the synthetic tidal records, to evaluate the feasibility of the regression-based method; validation against field measurement results remains to be conducted in the future.

## 3. Results

### 3.1 Spatial and temporal variation of AEP uncertainties

Following the guideline of IEC-62600-201 [24], we start from examining the AEP uncertainty from 90-day tidal current synthetic records (i.e., analyzing $\mathrm{dAEP}(s,\tau,d=90\ \text{days})$

304 as outlined in 2.2). Results are shown in Figure 3. The AEP uncertainty is shown by the 95%
305 range of AEP errors at each location of interest (Figure 3a, b). The upper bound (97.5%) and the
306 lower bound (2.5%) AEP uncertainty at each examined location shows the scale of AEP
307 uncertainty and how it is spatially dependent. Overall the AEP uncertainty associated with 90-
308 day records is between +/-15% along the U.S. east coast, California coast, and within Gulf of
309 Alaska, whereas the uncertainty is between -15% and +40% along Aleutian Islands, within Gulf
310 of Mexico and near Seattle.
311
312

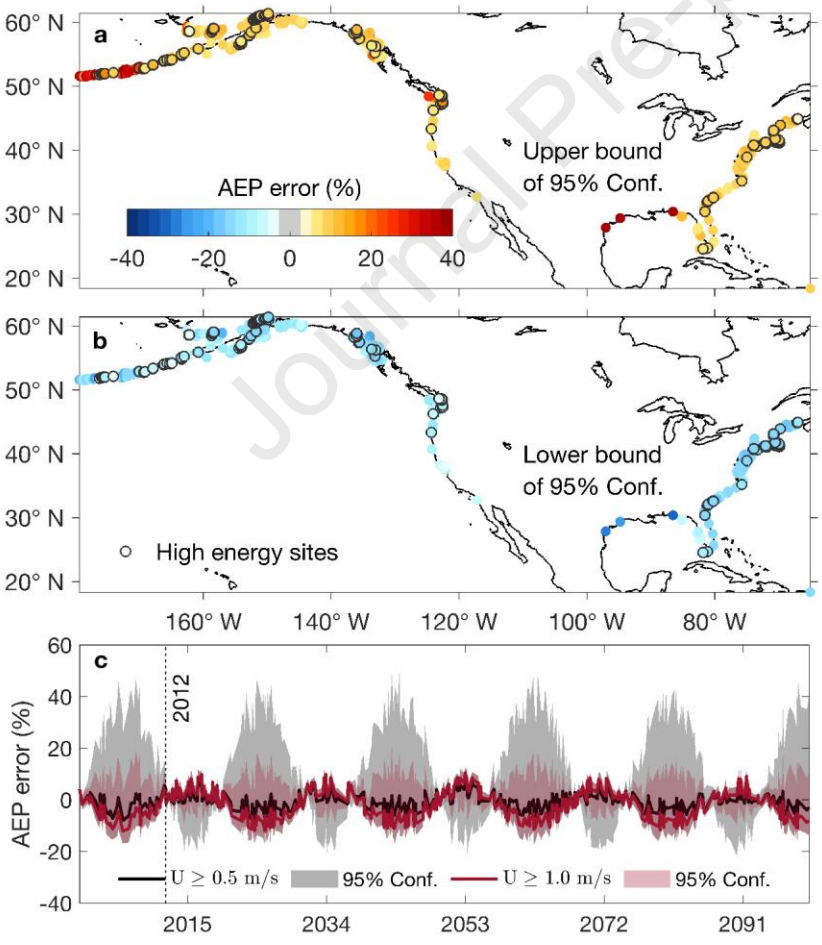


313

Figure 3. Spatial distribution and temporal variation of the AEP uncertainty (%) estimated from 90-day tidal current records. (a, b) Spatial distribution of AEP uncertainty, estimated as (a) the 97.5% and (b) the 2.5% AEP errors (i.e., 95% confidence interval) at each location. Circles with a black-colored outline mark the high energy locations. (c) AEP uncertainty as a function of time. Lines (shading) represent the average (the 95% range) AEP uncertainty. Black (red) is evaluated from the moderate (high) energy locations. Dashed line marks 2012, the reference year.

We also analyzed how the AEP uncertainty varies as we change the time periods (Figure 3c). Our result shows that the AEP uncertainty (shown by both the mean and the 95% confidence interval) has large low-frequency (decadal) and less high-frequency (monthly) variability, which is later found to be attributed to the lunar nodal cycle and the lunar spring-neap cycle, respectively. Comparing with the moderate energy locations (gray shading in Figure 3c), the AEP uncertainty of the high energy locations (pink shading) is smaller (cf. between +/-15% with -15% to 40%). The low frequency variability implies that the effect of the lunar nodal cycle must be factored into any long-term estimates of AEP.

### 3.2 Lunar nodal cycle effect on AEP assessment

Because all the time series include nodal corrections, to isolate the nodal cycle effect on AEP assessment, we adopted a recursive Gauss-Newton method (see Appendix), which fits a sinusoidal function to the temporally varying AEP errors. Each location is separately processed to find the amplitude and phase of the nodal fluctuation leading to minimum residual AEP errors. An example of fitting the sinusoidal function is shown in Figure 4a. At this example location, a large portion of the AEP uncertainty (total uncertainty is up to 35%) is due to the lunar nodal

337 cycle (red line in Figure 4a), as the residual AEP uncertainty (gray line) after removing the
338 contribution from the lunar nodal cycle has a much smaller percentage (less than 10%). We
339 apply this Gauss-Newton approach to obtain the portion of AEP uncertainty only associated with
340 the nodal cycle at each location of interest (Figure 4b, c; i.e., resulting in $\mathrm{dAEP}_{\mathrm{nodal}}(s, \tau, d = 90$
341 days), with subscript nodal denoting the portion of AEP error induced by nodal cycle). At the
342 majority of TEC locations, the scale of the nodal cycle contributed AEP uncertainties (Figure 4b,
343 c) is similar to the scale of the full AEP uncertainties (Figure 3a, b), suggesting that the nodal
344 cycle is a major source of AEP uncertainty when assessed from a 90-day measurement record.
345

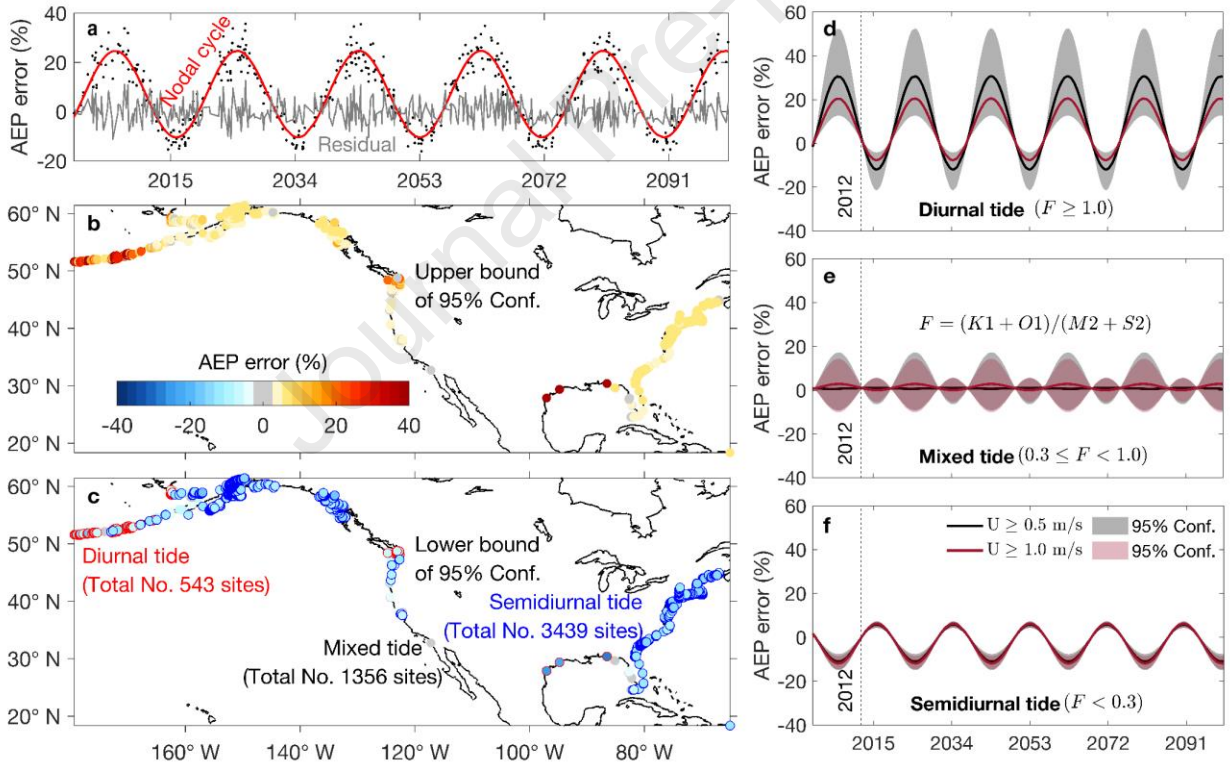

346

347 Figure 4. Spatial distribution and temporal variation of the AEP uncertainty (%) contributed by
348 the nodal cycle effect. (a) Illustration of identifying and isolating the nodal cycle contribution
349 (red line) from the full AEP uncertainties (dots) and showing the residual (gray line). (b, c)

Spatial distribution of the AEP uncertainty induced by the nodal cycle, with (b) showing the 97.5% and (c) the 2.5% AEP errors. In (c), the red circles mark the locations of diurnal tide (10.2% of all locations), the blue circles mark the semidiurnal tide (64.4%), and the remaining are mixed tide (25.4%). (d, e, f) AEP uncertainty induced by the nodal cycle, as a function of time, separately assessed based on the category of (d) diurnal, (e) mixed or (f) semidiurnal tides. The category is based on the major axis amplitude ratio between main diurnal and semidiurnal tidal constituents (equation listed in (e) and thresholds of each category marked at the bottom of (d, e, f)). Black (red) denotes the moderate (high) energy locations. Dashed line marks 2012, the reference year.

Moreover, consistent with previous studies [10, 11], we found that the location-dependent nodal modulation is linked to the characteristics of the tidal pattern, i.e., whether a location is characterized by diurnal, semidiurnal, or mixed tides. Tidal characteristics are determined by the form factor (e.g., [35]), $F$, a dimensionless number representing the ratio of tidal current constituents between the main diurnal and semidiurnal components, as followed,

$$F = \frac{K_1 + O_1}{M_2 + S_2}, \tag{9}$$

where $K_1$, $O_1$, $M_2$, and $S_2$ are the tidal major axis amplitudes. Then tides are classified as diurnal ($F \geq 1.0$), semidiurnal ($F < 0.3$), or mixed ($0.3 \leq F < 1.0$). Based on the classification, 10.2% moderate energy locations are featured by diurnal tides, mainly located along Aleutian Islands, within Gulf of Mexico and near Seattle; 64.4% locations are in semidiurnal form, located along the U.S. east coast, California coast and within Gulf of Alaska; 25.4% locations are mixed tides, and they are sporadically scattered along the coast (Figure 4c).

For each tidal category, we computed the AEP uncertainty associated with the nodal cycle. This is done by first isolating locations of a tidal form (e.g., $s =$ locations of diurnal tides) and calculating the statistics of $\mathrm{dAEP}_{\mathrm{nodal}}(s, \tau, d = 90 \text{ days})$ across those locations (Figure 4d-f). Semidiurnal tidal locations present a nodal modulation that last peaked in 2015, and will reach to maximum again in 2034, coinciding with the minimum lunar declination. Diurnal tidal locations show a nodal modulation that last peaked in 2006 and will peak again in 2025, coinciding with the maximum lunar declination. Mixed tides present the nodal modulation in between, hence having a maximum and a minimum in 2006, 2015, and so on. Our finding of the low frequency AEP uncertainty connected to the tidal forms is consistent with the equilibrium tidal theory, indicating that the nodal modulation of semidiurnal (diurnal) tides reaches a maximum when the lunar declination is at its minimum (maximum) [11].

### 3.3 Lunar spring-neap cycle effect on AEP assessment

Next we removed the nodal modulation from the full AEP errors (i.e., $\mathrm{dAEP}(s, \tau, d = 90 \text{ days}) - \mathrm{dAEP}_{\mathrm{nodal}}(s, \tau, d = 90 \text{ days})$). The residual AEP errors are relatively spatially uniform, with the uncertainty range overall smaller than the range induced by nodal cycle (cf. Figure 5a with Figure 4b). In this section, we show that the residual AEP uncertainty is mainly associated with the lunar spring-neap cycle.

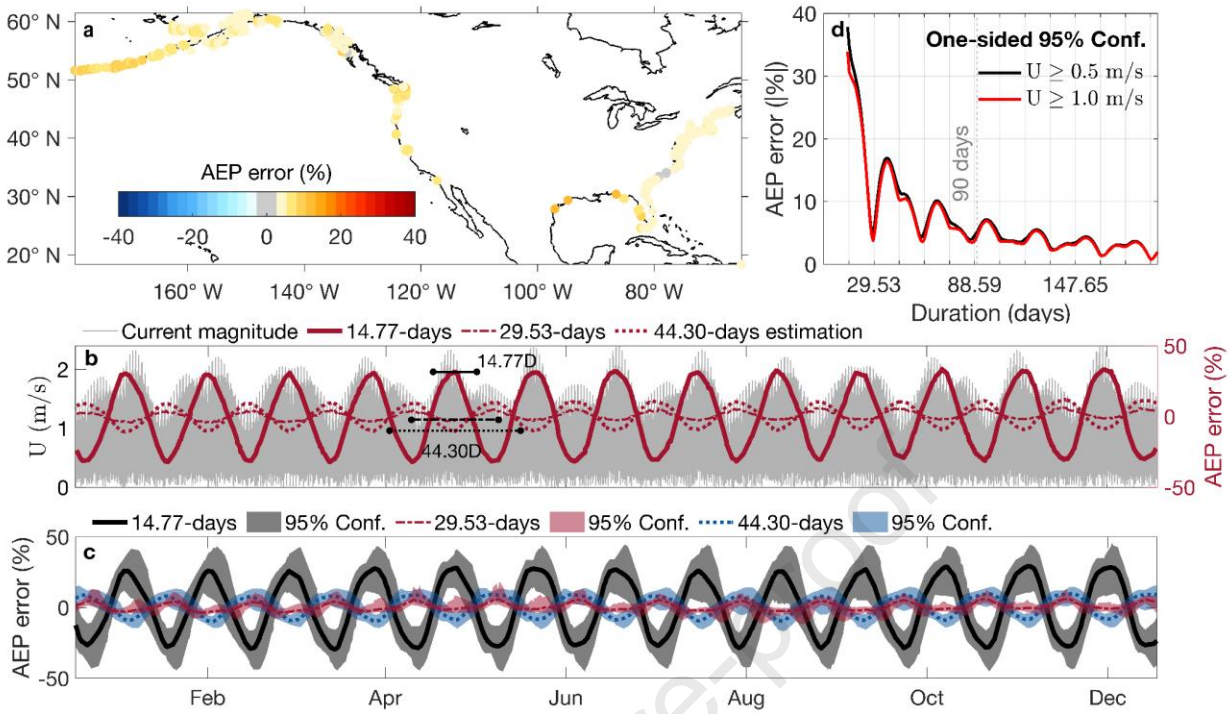


Figure 5. The AEP uncertainty (%) contributed by the lunar spring-neap cycle, fluctuated as the duration of the tidal current records varies. (a) Spatial distribution of the AEP uncertainty after removing the nodal cycle contribution. (b) An example location showing the AEP uncertainty assessed from 14.77- (solid red), 29.53- (dashed red) and 44.30-day (dotted red) tidal current records, as a function of the center time of those records. The gray line shows the current magnitude time series at the location. Line segments with endpoints mark the lengths of 14.77 (solid black), 29.53 (dashed black) and 44.30 days (dotted black) for reference. (c) Same as (b) except the analysis is expanded to all locations. Line and shading represent the mean and the 95% range across all locations. Black/red/blue corresponds to statistics of 14.77/29.53/44.30 days. (d) 95% absolute AEP uncertainty assessed from various durations, ranging from 14 to 196 days. Black (red) line is evaluated from moderate energy (high energy) locations. Gray dashed line marks the 90 days, the reference duration.

Note that the lunar spring-neap cycle operates on a frequency (i.e., 29.53 days) much higher than the nodal cycle. Thus, analysis based on our original 500 samples over a century may be enough to examine the low frequency variability (i.e., ~27 samples every 18 years), but may be too scarce to reflect the monthly-scale fluctuation (i.e., $< 1$ sample per month). This could explain why the residual AEP seems noisy over a century timeline (e.g., gray line of Figure 4a). To resolve the higher frequency variability, we randomly sampled another 500 timestamps during 2012 (i.e., ~42 samples per month) and calculated the AEP errors accordingly (i.e., an updated dAEP$(s, \tau, d)$ based on those timestamps, following the procedure of 2.2).

We then chose an example location, and show the AEP uncertainty assessed from 14.77-day, 29.53-day and 44.30-day tidal currents, corresponding to durations of 0.5, 1.0 and 1.5 lunar spring-neap cycles (Figure 5b). Among the three durations, the range of the AEP uncertainty is largest when AEP is evaluated from 14.77-day tidal currents, followed by 44.30-day and lastly 29.53-day records, suggesting that the AEP error does not monotonically decrease with increasing durations. More interestingly, when the AEPs assessed from 14.77-day tidal currents result in the maximum overprediction, the AEPs assessed from 44.30-day records result in the maximum underprediction. Comparing against the tidal current magnitude time series (gray line of Figure 5b), we find that the shift from over- to underprediction by extending the record durations is linked to the portion of tidal current speeds enclosed by the record durations. A 14.77-day time period may collect a high tide record (solid black line segment), whereas a 44.30-day time period extended from that 14.77-day period (dotted black line segment) includes a larger portion of lower tides, hence the overprediction (up to 30% AEP assessment error) and underprediction (up to 12% AEP assessment error), respectively. Any 29.53-day time period, on

the other hand, collects a relatively full range of tidal currents, hence leading to smallest AEP errors (at most 6% AEP assessment error) among the three durations.

For a robust assessment, we expand from analyzing one location to incorporate all locations, by calculating the mean and the 95% range of AEP uncertainty across all locations (Figure 5c). We find that the AEP uncertainty assessed from 14.77-day tidal currents is consistently higher than those evaluated from 44.30-day records, followed by 29.53-day records. Moreover, the peak overprediction from 14.77-day records and the peak underprediction from 44.30-day tidal currents are consistently in phase. These results support our findings based on one location, i.e., how the AEP error is sensitive to the portion of tidal currents captured by a measurement period.

To better understand how the effect of lunar spring-neap cycle translates into the sensitivity to the measurement durations, we examined the AEP uncertainty as a function of durations, ranging from 14 to 196 days (Figure 5d; i.e., computing the 95% value based on the long vector of the absolute AEP errors, $|\mathrm{dAEP}(s, \tau, d)|$, for a given $d$). The AEP uncertainty assessed from a 14-day record is the largest, ~35%. As the duration increases from 14 days to 29.53 days, the AEP error gradually decreases, reaching to a local minimum of ~5%. The AEP error starts to increase for durations longer than 29.53 days, but drops again to ~4.6% for duration of 59.06 days. Overall, the AEP uncertainty shows an oscillation with a frequency of lunar spring-neap cycle and a decaying magnitude as durations increase, which corroborates with our previous finding that the AEP uncertainty is minimized for fully resolving lunar spring-neap cycles and is maximized when a lunar spring-neap cycle is partially resolved.

### 3.4 Lunar spring-neap cycle effect on array AEP assessment

We have examined the uncertainty of AEP associated with single TEC deployment, directly computed using tidal currents with a short-record. Although these analyses assume a single TEC

deployment, they are easily applicable to the expensive scenario of multiple bottom-mounted current profilers for assessing a TEC array. Alternatively, here we evaluate a cost-effective strategy for assessing array AEPs (as outlined in 2.3; Figure 2): (a) a long-term FI measurement of tidal currents at one location of the TEC array; (b) MV measurements collecting short records at the other locations; (c) the long-term records for each of these other locations are then inferred from the FI record through regression, and later used for computing the array AEP. Note that we assume that the FI measurement has a full-year tidal record (i.e., minimizing the uncertainties linked to the FI measurement), in order to evaluate the uncertainty of AEP errors linked to the inferred method or the MV measurement.

Yet with the full-year record, there is still one remaining source of AEP error pertaining to the FI measurement: the choice of FI measurement location among the TEC array (Figure 6c). We hypothesize that the FI measurement is better placed at the highest energy location, rather than lowest energy, as the highest energy location contains the largest variation of tidal currents and thus might be a more suitable source for predicting nearby less energetic locations. The second hypothesis is that the FI measurement is better placed at the center of the arrays, rather than the corner, as the center position is more likely to have similar flow fields to its nearby locations and thus might be beneficial for regression, which inherently relies on such similarity. The method will be sensitive to spatial gradients in the flow field, particularly if there is a phase shift in the timing of the flow; however, if a linear relationship exists because the two sites are relatively in phase, the method can still be successful. We tested the two hypotheses by setting the FI measurement at the max or the min energy position, the center or the corner of the TEC arrays. As expected, compared with the min energy position or the corner of the array, setting the max energy location or the center of the array as the FI measurement results in a much smaller

range of AEP errors. (Note that here we analyze dAEPs$(a, \tau, d, q)$ associated with different FI deployment locations, while assuming $q$ is the tidal current magnitude time series and $d$ is either 12 or 25 hours.) This suggests that the regression-based AEP assessment is likely more accurate, when the TEC array is designed such that the highest energy location is at the center and the FI measurement is placed at that location.

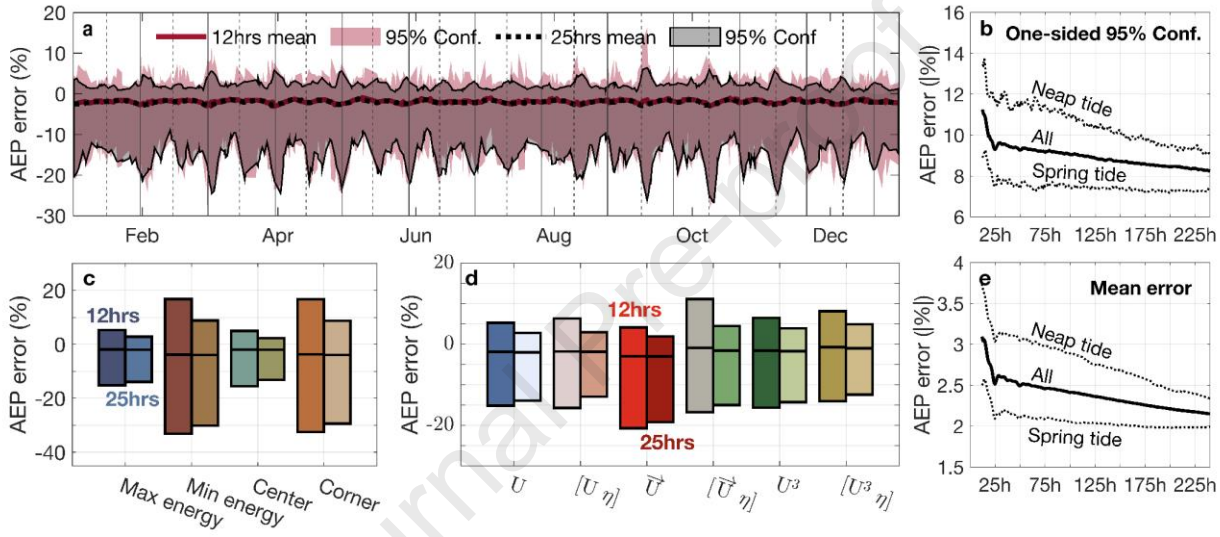


Figure 6. AEP uncertainty (%) of TEC arrays sensitive to spring-neap tide, the tidal energy magnitude and locations of the FI measurements in the arrays, and various regression modeling frameworks. (a) AEP errors assessed from the 12- (red), and 25-hours (black) tidal currents of MV measurement, as a function of time. Line is the average, and the shading is the 95% confidence interval of all TEC arrays. Vertical gray solid and dashed lines mark the dates of neap tide. (b, e) AEP uncertainty assessed from various durations of MV measurements, ranging from 12 to 240 hours, with (b) plotting the 95% absolute AEP errors and (e) plotting the mean. Black line is evaluated from all examined time periods; top (bottom) dashed line is evaluated from neap (spring) tide time periods. (c) Boxplot showing the mean (middle lines) and the 95% confidence interval (from top to the bottom of bars) AEP errors, assuming that the FI measurement is placed

at highest vs. lowest mean current magnitude position, and center vs. corner of the arrays. For each category of the FI measurement positions, the examined durations of the MV measurement are 12 (left bars of each category) and 25 (right bars) hours. (d) Same as (c) except for testing different inputs of the regression models, including current magnitudes, current magnitudes and water levels, currents with real zonal components and imaginary meridional components, currents and water levels, cubic current magnitudes, cubic current magnitudes and water levels.

We then evaluated the sensitivity of the AEP assessment to the various frameworks of the inferred method. Options for the different frameworks include whether to predict the complex tidal current vectors, the tidal current magnitudes, or the cubic current magnitudes, and whether to incorporate the water levels in the input (Figure 6d; detail illustrated in 2.3). Among these options, building the regression solely based on the tidal current magnitude time series (first two bars of Figure 6d), one of the simplest frameworks, might be a robust option. (Note that here we analyze how dAEPs$(a, \tau, d, q)$ varies with different $q$, while assuming FI measurement is taken at the max energy location and $d$ is either 12 or 25 hours.)

Following these sensitivity analyses, we establish a robust baseline - constructing the modeling framework using tidal current magnitude time series and assuming the FI measurement taken at the max energy location of the TEC arrays (i.e., the dAEPs$(a, \tau, d, q)$ is reduced to dAEPs$(a, \tau, d)$). Based on this baseline, we examine the AEP uncertainty as a function of time as well as the durations of the measurement periods (Figure 6a). We are mainly interested in two durations, 12 or 25 hours, considering that shorter durations of mobile survey are easier to implement. We find that those 12-hr MV measurement in general leads to noisier AEP assessment and larger AEP assessment uncertainty than conducting the 25-hr MV measurement (Figure 6a). This is also seen in Figure 6c, d. We further examine this by evaluating the AEP

uncertainty linked to a wide range of MV measurement durations, from 12 to 240 hours (solid line of Figure 6b, e). We find the AEP uncertainty rapidly decreases as the MV measurement duration increases from 12 to 25 hours, and then slowly decreases for durations longer than 25 hours. Our results are similar to other results in the literature (e.g. [36]), which suggest at least 24-hr mobile surveys to capture the minimum tidal harmonics.

More interestingly, the temporal variation of the AEP errors shows a clear fluctuation with respect to spring-neap cycle (Figure 6a). Specifically, the AEP errors reach local extremes when the MV measures neap tides (vertical solid and dashed lines in Figure 6a). In contrast, the range of AEP errors is the smallest when measuring spring tides (in between vertical lines). A larger range of AEP errors during neap tides and a smaller range of AEP errors during spring tides, whether we assume 12-hr or 25-hr MV measurement, is always present. Moreover, we find that the AEP evaluated from spring tides is rigorously better than from neap tides, for any durations of interest (dashed lines of Figure 6b, e). These results support that the array AEP errors evaluated from hours of MV measurements coupled with longer term FI measurements are largely associated with the spring-neap cycles.

Lastly, through optimizing the choice of FI measurement, the modelling framework, the duration of MV measurement, and the time period to collect tidal record, our proposed indirect measurement scheme shows a relatively steady mean AEP uncertainty of -3% (Figure 6a, e). Out of the 127 TEC arrays, only 5% of the TEC arrays still show AEP uncertainty greater than 10% (Figure 7), suggesting that the strategy of regressing a FI measurement onto nearby MV measurements is a viable option.

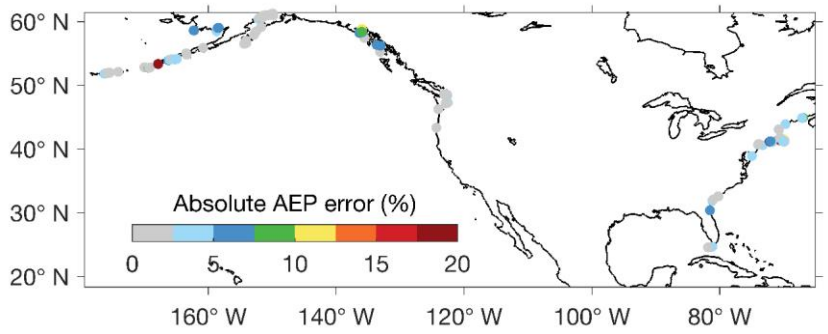


Figure 7. Spatial distribution of the 95% absolute AEP uncertainty, by setting FI measurement at maximum energy of the TEC array, assuming 25-hour MV measurement during spring tides, and using current magnitude time series for regression.

## 4. Discussion and Conclusion

The availability of measured tidal current records is scarce, especially when compared to in-situ water levels [30]. To work around this limitation, in this study we utilize the U.S. tidal database containing tidal harmonics of millions of locations, for the advantage of generating tidal records for any time periods at a large quantity of locations. This allows us to rigorously examine the uncertainty of the AEP assessment linked to short tidal current records, and to provide comprehensive understanding of source of errors and impact.

However, generating short tidal records based on tidal harmonics results in pure tidal time series, and the AEP uncertainty derived from these pure tides therefore does not resolve the impact from any non-astronomical sources. These sources may include weather related effects, such as storm surges, waves, and climatic seasonal variability. Thus, without incorporating non-tidal effects, we acknowledge that the scale of the AEP errors may have been underestimated, compared to the AEP uncertainty analyzed from in-situ current time series. On the other hand, it is possible to collect current data during time periods of calm synoptic conditions [37], thereby

restricting the non-tidal factors to be less influential and more comparable with numerical model-derived AEP.

The use of boat-based MV measurements for capturing flow structure and velocity distributions in open channel flows, such as rivers, is not uncommon [38-46]. This approach aims to collect data while the boat is moving, hence, only one data point is typically obtained in each location along the boat path (a current profiler typically has a sampling rate of 1 or 2 Hz). This approach is useful for mapping the velocity and calculating flow discharge in a river cross-section. Several factors such as the stochastic nature of flow in rivers in which the flow discharge changes quickly over time, the high variability of bathymetry and topography within a relatively short distance, and coupled with the inherent technical limitation of current profilers (diverging acoustic beams, measuring in inhomogeneous flow, Doppler noise), often contribute to the uncertainty of the current measurements significantly at riverine sites [47, 48]. The MV measurements proposed for this project is different from the approach typically used in river applications. The approach taken here is to essentially take a longer measurement (e.g., 5 minutes, which typically equivalent to 300-600 data points) at each station, and use the time-averaged velocity at each station to significantly reduce random error [40, 48, 49]. This time-averaged velocity, which removes instantaneous velocity fluctuations, are comparable to that obtained from numerical models, such as ROMS. In a tidal environment, a time averaging window between 3 and 5 min is generally sufficiently long enough for minimizing the variations caused by large-scale eddies, while at the same time is short enough for ensuring the current speed within this time period is relatively unaffected by periodic changes of tidal velocity magnitude [18]. Additionally, at tidal sites, the contribution of these factors is expected to be less

572 significant, because unlike the stochastic nature of the flow in rivers, tidal flow is highly
573 predictable.

574 With the synthetic tidal records of various time periods and multiple sites, we examine the
575 role of astronomical factors on the short-record induced AEP uncertainty. These astronomical
576 factors include the 18.61 years nodal cycle effect and 29.51 days spring-neap cycle effect. We
577 find that an astronomical factor affects the AEP evaluation such that it fluctuates in the same
578 frequency as the astronomical cycle. As tidal currents are a combined result of various tidal
579 harmonics, the AEP uncertainty also includes the combined effect of different astronomical
580 impacts. With each astronomical impact separately examined, we present a schematic diagram
581 (Figure 8) to summarize the portion of AEP uncertainty linked to each astronomical factor and
582 how the portion varies with the measurement time scale.

583

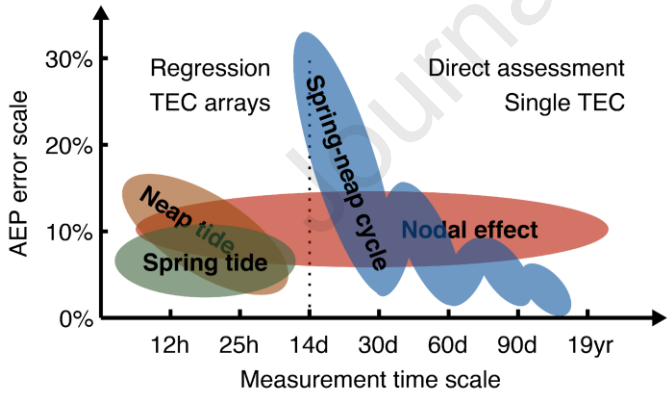


584

585 Figure 8. Schematic diagram summarizing AEP error scales linked to different physical
586 processes, how they are represented in measurement time scales and in the methods of being
587 evaluated. Physical processes including spring-neap cycle and nodal cycle. Methods include
588 evaluating TEC arrays based on regression when measurement time scale is less than 14 days,
589 and evaluating the single TEC directly when measurement is longer.

590

591 The lunar spring-neap cycle is a critical factor that contributes to a significant AEP
592 uncertainty, up to 33% uncertainty when the measurement duration is one half of the cycle, i.e.,
593 14.76 days. In general, the uncertainty decreases in an oscillating manner as a function of
594 measurement duration, and is at its local minima when the record period is an exact multiple of
595 the lunar spring-neap cycle, i.e., $1 \times 29.51$ days, $2 \times 29.51$ days, and etc. In contrast, the
596 uncertainty is at its local maxima when the record period is an exact multiple of the lunar spring-
597 neap cycle plus one half of the lunar spring-neap cycle, i.e., $1.5 \times 29.51$ days, $2.5 \times 29.51$ days.
598 This observation suggests that resolving a full tidal current variation in the exact length of a lunar
599 spring-neap cycle provides a more accurate representation of the long-term tidal current
600 statistics. In addition, when the available record of data is longer than an exact multiple of the
601 lunar cycle, we recommend to cut off the length of the record for AEP analysis to an exact
602 multiple of the lunar cycle, to reduce the uncertainty in AEP calculation.
603 The lunar nodal-cycle induced AEP errors are in the order of ~10%. We emphasize that, on a
604 measurement time scale much shorter than a nodal cycle, the portion of AEP errors linked to the
605 nodal cycle still exists, however not apparent from the appearance of short tidal current records.
606 Thus, we recommend to account for the contribution from the lunar nodal cycle, especially
607 during the strong nodal effect years, such as the year 2025 and the year 2034. Notably,
608 accounting for the nodal effect requires prior-knowledge of the multi-decadal tidal time series,
609 which is not readily available in the fieldwork. This can be accomplished by processing the
610 collected tidal time series by T-TIDE, obtaining the tidal harmonics, and simulating the long-
611 term tidal time series for identifying the nodal contribution.

612 If the measurement at a location is only on a time scale of hours, we propose that the AEP is
613 assessed from an inferred tidal record, projected from a long-term tidal record of a nearby
614 location based on the two locations' co-variability. On these extremely short measurement time
615 scales, the bi-weekly variation of a spring-neap cycle has a prominent impact on the AEP
616 uncertainty. Specifically, the short record measurement taken during spring tide leads to a more
617 accurate estimation of AEP with less uncertainty, compared with measurement taken during neap
618 tide. This is likely associated with tidal variation during spring tide being much larger than
619 during neap tide, hence providing relatively "fuller" range of tides to be captured by regression.
620 Note that in this study, we assume a continuous MV measurement (e.g., measuring 12 or 25
621 hours nonstop), which in the fieldwork is not always feasible. However, it is plausible to
622 effectively extend the lengths of MV measurement, such as measuring 8 hours for 3 consecutive
623 days. For the purpose of capturing a fuller range of tidal variation, there might be a difference,
624 e.g., between measuring 3 days during 3 different spring tide periods, or measuring 2 days during
625 spring tide and 1 day during neap tide, etc. Whether there is an optimal strategy for the number
626 of days and the corresponding periods of measurement is to be investigated in a different follow-
627 up study, where we will also examine the actual FI and MV measurement time series collected in
628 the field following the guidelines of this study. Lastly, we emphasize that, despite the difference
629 of AEP uncertainty for MV measurement during spring and neap tide, the mean AEP uncertainty
630 across 127 sets of TEC arrays is only 3%, hence the robustness of the inferred method.
631 Lastly, the inferred method of choice is a least square regression, evaluated directly on tidal
632 records rather than tidal harmonics. A classic tidal harmonic analysis applies least square fitting
633 to find the amplitude, the inclination and the phase of a known-frequency tidal constituent. Yet,
634 under the circumstances of hours measurement, fitting tidal harmonics directly requires solving

an underdetermined system, i.e., more unknowns than equations. Thus, we evaluate the least square regression on the tidal record directly, i.e., solving a statistically robust overdetermined system. The resulting AEP error is reasonable and thus supports such an inferred method.

Overall, our result corroborates and extends from the recommendation of IEC-62600-201. For single TEC deployments, we recommend a 90 days measurement for projects with economical flexibility, and an exact 30 days measurement for projects with a tight budget. For TEC arrays using our inferred scheme, we recommend collecting FI measurement following the guidelines for the single TEC deployment and conducting MV measurement during spring tide for an effective length of 25 hours. In both scenarios, the nodal cycle effect can be isolated by processing the long-term measured or inferred tidal current records in T-TIDE. In summary, our study helps provide guidelines on how to optimally choose measurement time periods, under what circumstances to apply direct assessment or regression assessment, what to expect on the scale of AEP errors and the astronomical sources leading to such AEP errors.

**Acknowledgements**

This work is funded in part or whole by the U.S. Department of Energy Water Power Technologies Office, through the Marine Energy Seedlings Program.

Sandia National Laboratories is a multi-mission laboratory managed and operated by National Technology and Engineering Solutions of Sandia, LLC, a wholly owned subsidiary of Honeywell International, Inc., for the U.S. Department of Energy's National Nuclear Security Administration under contract DE-NA0003525. This manuscript describes objective technical results and analysis. Any subjective views or opinions that might be expressed in the paper

do not necessarily represent the views of the U.S. Department of Energy or the United States Government.

## Appendix

A Recursive Gauss-Newton Method

The recursive Gauss-Newton algorithm is commonly applied to solve nonlinear least square problems. In this study, given a time series of AEP error, the method is used to fit a sinusoidal function and find the amplitude, the frequency, the phase and the constant bias that leads to the least square error between the fitted and the original time series. We first assume a general form of sinusoidal function,

$$w(\tau) = c_1 \sin(2\pi \cdot c_2 \cdot \tau + c_3) + c_4 \quad \text{(A.1)}$$

where $c_1$ is the amplitude, $c_2$ is the frequency, $c_3$ is the phase, and $c_4$ is the constant bias. $w(\tau)$ is a vector, equivalent to temporal variation of dAEP$(s, \tau, d = 365$ days) at a location $s$. The derivative with respect to $c_1$, $c_2$, $c_3$, $c_4$, is as followed,

$$\frac{\partial w}{\partial c_1} = \sin(2\pi \cdot c_2 \cdot \tau + c_3), \quad \text{(A.2)}$$

$$\frac{\partial w}{\partial c_2} = c_1 \cdot 2\pi \cdot \tau \cos(2\pi \cdot c_2 \cdot \tau + c_3), \quad \text{(A.3)}$$

$$\frac{\partial w}{\partial c_3} = c_1 \cos(2\pi \cdot c_2 \cdot \tau + c_3), \quad \text{(A.4)}$$

$$\frac{\partial w}{\partial c_4} = \mathbf{1}. \quad \text{(A.5)}$$

This forms a Jacobian matrix of $\mathbf{J} = \left[\frac{\partial w}{\partial c_1} \quad \frac{\partial w}{\partial c_2} \quad \frac{\partial w}{\partial c_3} \quad \frac{\partial w}{\partial c_4}\right]$. The update direction of the iteration is determined as,

$$\Delta = (\mathbf{J}^{\mathrm{T}}\mathbf{J})^{-1}\left(\mathbf{J}^{\mathrm{T}}\left(w(\tau) - \widehat{w}(\tau)\right)\right), \quad \text{(A.6)}$$

where $\widehat{w}(\tau)$ is the fitted time series. The iteration starts from initializing parameters, $\mathbf{c} = [c_1 \quad c_2 \quad c_3 \quad c_4]^{\mathrm{T}}$ and evaluating $\widehat{w}(\tau)$, $\mathbf{J}$ and $\Delta$ accordingly. The estimated parameters of next step are then determined by the update rule,

$$\mathbf{c}^{k+1} = \mathbf{c}^{k} + \lambda \cdot \Delta^{k}, \quad \text{(A.7)}$$

where the superscript $^{k}$ represents the iteration step and $\lambda$ is a small-value constant, denoting a small step toward the iteration direction (in this study, we take $\lambda = 0.001$). By recursively updating $\mathbf{c}$, we eventually arrive at a set of parameters leading to minimum least square error, i.e., solving $\arg\min_{\mathbf{c}} \frac{1}{2}\|w(\tau) - \widehat{w}(\tau)\|_2^2$. The $\widehat{w}(\tau)$ time series evaluated based on the optimal parameters is thus the nodal cycle contributed AEP error.

# REFERENCES


[1] International Energy Agency (IEA), Global Energy Review 2021, IEA, Paris, https://www.iea.org/reports/global-energy-review-2021 (2021).

[2] The Intergovernmental Panel on Climate Change (IPCC), Global Warming of 1.5°C. An IPCC Special Report on the impacts of global warming of 1.5°C above pre-industrial levels and related global greenhouse gas emission pathways, in the context of strengthening the global response to the threat of climate change, sustainable development, and efforts to eradicate poverty, [Masson-Delmotte, V., P. Zhai, H.-O. Pörtner, D. Roberts, J. Skea, P.R. Shukla, A. Pirani, W. Moufouma-Okia, C. Péan, R. Pidcock, S. Connors, J.B.R. Matthews, Y. Chen, X. Zhou, M.I. Gomis, E. Lonnoy, T. Maycock, M. Tignor, and T. Waterfield (eds.)]. In press. (2018).

[3] T. Kurbatova, T. Perederii, Global trends in renewable energy development, 2020 IEEE KhPI Week on Advanced Technology (KhPIWeek), 2020, pp. 260-263.

[4] M.Z. Jacobson, M.A. Delucchi, Z.A.F. Bauer, S.C. Goodman, W.E. Chapman, M.A. Cameron, C. Bozonnat, L. Chobadi, H.A. Clonts, P. Enevoldsen, J.R. Erwin, S.N. Fobi, O.K. Goldstrom, E.M. Hennessy, J. Liu, J. Lo, C.B. Meyer, S.B. Morris, K.R. Moy, P.L. O'Neill, I. Petkov, S. Redfern, R. Schucker, M.A. Sontag, J. Wang, E. Weiner, A.S. Yachanin, 100% Clean and Renewable Wind, Water, and Sunlight All-Sector Energy Roadmaps for 139 Countries of the World, Joule 1(1) (2017) 108-121.

[5] A.C. Duxbury, A.B. DUXBURY, Fundamentals of oceanography, (1992).
[6] F.O. Rourke, F. Boyle, A. Reynolds, Tidal energy update 2009, Appl Energ 87(2) (2010) 398-409.
[7] J. Widen, N. Carpman, V. Castellucci, D. Lingfors, J. Olauson, F. Remouit, M. Bergkvist, M. Grabbe, R. Waters, Variability assessment and forecasting of renewables: A review for solar, wind, wave and tidal resources, Renew Sust Energ Rev 44 (2015) 356-375.
[8] E.P. Kvale, The origin of neap–spring tidal cycles, Marine Geology 235(1) (2006) 5-18.
[9] C.A. Kaye, G.W. Stuckey, Nodal tidal cycle of 18.6 yr.: its importance in sea-level curves of the east coast of the United States and its value in explaining long-term sea-level changes, Geology 1(3) (1973) 141-144.
[10] I.D. Haigh, M. Eliot, C. Pattiaratchi, Global influences of the 18.61 year nodal cycle and 8.85 year cycle of lunar perigee on high tidal levels, Journal of Geophysical Research-Oceans 116 (2011).
[11] D.J. Peng, E.M. Hill, A.J. Meltzner, A.D. Switzer, Tide Gauge Records Show That the 18.61-Year Nodal Tidal Cycle Can Change High Water Levels by up to 30cm, Journal of Geophysical Research-Oceans 124(1) (2019) 736-749.
[12] S.P. Neill, A. Angeloudis, P.E. Robins, I. Walkington, S.L. Ward, I. Masters, M.J. Lewis, M. Piano, A. Avdis, M.D. Piggott, G. Aggidis, P. Evans, T.A.A. Adcock, A. Zidonis, R. Ahmadian, R. Falconer, Tidal range energy resource and optimization - Past perspectives and future challenges, Renewable Energy 127 (2018) 763-778.
[13] R.H. Charlier, Forty candles for the Rance River TPP tides provide renewable and sustainable power generation, Renewable and Sustainable Energy Reviews 11(9) (2007) 2032-2057.
[14] S. Waters, G. Aggidis, Tidal range technologies and state of the art in review, Renewable and Sustainable Energy Reviews 59 (2016) 514-529.
[15] C. Wang, History, Current state and prospect of the development of ocean energy in China, Proceedings of International Ocean Energy Symposium (IOES-2009). Harbin, China, 2009.
[16] Y.H. Bae, K.O. Kim, B.H. Choi, Lake Sihwa tidal power plant project, Ocean Eng 37(5) (2010) 454-463.
[17] J.A. Colby, M.A. Adonizio, P.C.V. Power, Hydrodynamic analysis of kinetic hydropower arrays, Waterpower XVI 204 (2009).
[18] B. Gunawan, V.S. Neary, J. Colby, Tidal energy site resource assessment in the East River tidal strait, near Roosevelt Island, New York, New York, Renewable Energy 71 (2014) 509-517.
[19] Y. Li, H. Liu, Y. Lin, W. Li, Y. Gu, Design and test of a 600-kW horizontal-axis tidal current turbine, Energy 182 (2019) 177-186.
[20] M. Nachtane, M. Tarfaoui, I. Goda, M. Rouway, A review on the technologies, design considerations and numerical models of tidal current turbines, Renewable Energy 157 (2020) 1274-1288.
[21] Orbital Marine Power, World's most powerful tidal turbine, the O2, starts exporting clean power, https://orbitalmarine.com/o2-power-generation/.
[22] E. Fagan, Y. Jiang, A. Kazemi, J. Goggins, Design and testing of a full-scale 2 MW tidal turbine blade, 2019.
[23] C. Legrand, Assessment of tidal energy resource: Marine renewable energy guides, European Marine Energy Centre2009.

[24] International Electrotechnical Commission Technical Specification (IEC TS 62600-201), Marine Energy: Wave, Tidal and Other Water Current Converters. Tidal Energy Resource Assessment and Characterization, 2015.
[25] B. Tajfirooz, M. Ezam, A.A. Bidokhti, K. Lari, Evaluation of probabilistic and deterministic methods for estimating energy potential of tidal currents in the Khuran Strait, the Persian Gulf, Int J Environ Sci Te 17(3) (2020) 1727-1738.
[26] S. Radfar, R. Panahi, T. Javaherchi, S. Filom, A.R. Mazyaki, A comprehensive insight into tidal stream energy farms in Iran, Renew Sust Energ Rev 79 (2017) 323-338.
[27] B. Polagye, J. Thomson, Tidal energy resource characterization: methodology and field study in Admiralty Inlet, Puget Sound, WA (USA), Proceedings of the Institution of Mechanical Engineers, Part A: Journal of Power and Energy 227(3) (2013) 352-367.
[28] J. Thiébot, S. Guillou, E. Droniou, Influence of the 18.6-year lunar nodal cycle on the tidal resource of the Alderney Race, France, Applied Ocean Research 97 (2020) 102107.
[29] J. Thiébot, N. Guillou, D. Coles, S. Guillou, On nodal modulations of tidal-stream energy resource in north-western Europe, Applied Ocean Research 121 (2022) 103091.
[30] D.S. Byun, D.E. Hart, Predicting Tidal Currents Using 25-h Observations through a Complete Tidal Species Modulation with Tidal Current Constant Corrections Method, J Atmos Ocean Tech 35(12) (2018) 2405-2420.
[31] Z. Defne, K.A. Haas, H.M. Fritz, L.D. Jiang, S.P. French, X. Shi, B.T. Smith, V.S. Neary, K.M. Stewart, National geodatabase of tidal stream power resource in USA, Renew Sust Energ Rev 16(5) (2012) 3326-3338.
[32] D.B. Haidvogel, H. Arango, W.P. Budgell, B.D. Cornuelle, E. Curchitser, E. Di Lorenzo, K. Fennel, W.R. Geyer, A.J. Hermann, L. Lanerolle, J. Levin, J.C. McWilliams, A.J. Miller, A.M. Moore, T.M. Powell, A.F. Shchepetkin, C.R. Sherwood, R.P. Signell, J.C. Warner, J. Wilkin, Ocean forecasting in terrain-following coordinates: Formulation and skill assessment of the Regional Ocean Modeling System, J Comput Phys 227(7) (2008) 3595-3624.
[33] R. Pawlowicz, B. Beardsley, S. Lentz, Classical tidal harmonic analysis including error estimates in MATLAB using T-TIDE, Comput Geosci-Uk 28(8) (2002) 929-937.
[34] A.S. Bahaj, L.E. Myers, Fundamentals applicable to the utilisation of marine current turbines for energy production, Renewable Energy 28(14) (2003) 2205-2211.
[35] O. Artal, O. Pizarro, H.H. Sepulveda, The impact of spring-neap tidal-stream cycles in tidal energy assessments in the Chilean Inland Sea, Renewable Energy 139 (2019) 496-506.
[36] Valle-Levinson, A., Huguenard, K., Ross, L., Branyon, J., MacMahan, J., & Reniers, A. (2015). Tidal and nontidal exchange at a subtropical inlet: Destin Inlet, Northwest Florida. Estuarine, Coastal and Shelf Science, 155, 137-147.
[37] D.-S. Byun, D.E. Hart, Predicting Tidal Heights for New Locations Using 25 h of in situ Sea Level Observations plus Reference Site Records: A Complete Tidal Species Modulation with Tidal Constant Corrections, J Atmos Ocean Tech 32(2) (2015) 350-371.
[38] R.L. Dinehart, J.R. Burau, Averaged indicators of secondary flow in repeated acoustic Doppler current profiler crossings of bends, Water Resour Res 41(9) (2005).
[39] R.L. Dinehart, J.R. Burau, Repeated surveys by acoustic Doppler current profiler for flow and sediment dynamics in a tidal river, J Hydrol 314(1-4) (2005) 1-21.
[40] J. Le Coz, G. Pierrefeu, M. Jodeau, A. Paquier, Mean vertical velocity profiles from aDcp river discharge measurement datasets, Proceedings 32nd Congress of International Association of Hydraulic Engineering and Research, Venice, Italy., 2007, p. 10.

792 [41] R.N. Szupiany, M.L. Amsler, J.L. Best, D.R. Parsons, Comparison of fixed- and moving-
793 vessel flow measurements with an aDp in a large river, J Hydraul Eng 133(12) (2007) 1299-
794 1309.
795 [42] B. Gunawan, M. Sterling, D.W. Knight, Using an acoustic Doppler current profiler in a
796 small river, Water Environ J 24(2) (2010) 147-158.
797 [43] B. Gunawan, X. Sun, M. Sterling, K. Shiono, R. Tsubaki, P. Rameshwaran, D.W. Knight,
798 J.H. Chandler, X. Tang, I. Fujita, The application of LS-PIV to a small irregular river for inbank
799 and overbank flows, Flow Measurement and Instrumentation 24 (2012) 1-12.
800 [44] V.S. Neary, B. Gunawan, C. Hill, L.P. Chamorro, Near and far field flow disturbances
801 induced by model hydrokinetic turbine: ADV and ADP comparison, Renewable Energy 60
802 (2013) 1-6.
803 [45] V.S. Neary, B. Gunawan, D.C. Sale, Turbulent inflow characteristics for hydrokinetic
804 energy conversion in rivers, Renew Sust Energ Rev 26 (2013) 437-445.
805 [46] B. Gunawan, V.S. Neary, J. Mortensen, J.D. Roberts, Assessing and Testing Hydrokinetic
806 Turbine Performance and Effects on Open Channel Hydrodynamics: An Irrigation Canal Case
807 Study, Sandia National Lab.(SNL-NM), Albuquerque, NM (United States), 2017.
808 [47] B. Gunawan, V.S. Neary, C. Hill, Comparing fixed-vessel and moving-vessel ADCP
809 measurements in a large laboratory flume, J Hydraul Eng 143(5) (2017) 06017001.
810 [48] M. Muste, K. Yu, M. Spasojevic, Practical aspects of ADCP data use for quantification of
811 mean river flow characteristics; Part 1: moving-vessel measurements, Flow Measurement and
812 Instrumentation 15(1) (2004) 1-16.
813 [49] Palodichuk, Michael, Brian Polagye, and Jim Thomson. "Resource mapping at tidal energy
814 sites." IEEE Journal of Oceanic Engineering 38.3 (2013): 433-446.
815

**Declaration of interests**

☒ The authors declare that they have no known competing financial interests or personal relationships that could have appeared to influence the work reported in this paper.

☐ The authors declare the following financial interests/personal relationships which may be considered as potential competing interests: